A Noncontact Fall Detection Method for Bedside Application With a MEMS Infrared Sensor and a Radar Sensor

Chunhua He, Shuibin Liu, Guangxiong Zhong, Heng Wu, Lianglun Cheng, Guizhen Yan, and Yangxing Wen

***Abstract*—With the rapid development of economy, science, and technology, the aging issues become more and more serious. People aged above 65 have a risk of 28%–35% to fall. Among them, bedside falls happen most frequently. Therefore, the capability to detect fall events of the elderly is very important. In this article, a novel noncontact fall detector based on a MEMS low-resolution infrared sensor and a low-cost radar sensor is developed to detect bedside fall. Besides, IR image processing algorithms based on the adaptive filter, successive approximation, double boundary scans, and mathematical morphology processing are proposed in detail. Partition processing algorithm is used to suppress the influence of residual or existed heat sources on the bed or ground. Then, the statistical features of the center, area, temperature and duration, as well as stable flag and fall action flag, are extracted for fall recognition. Finally, a three-layer radial basis function neural network is applied to distinguish the fall events from the nonfall events. Considering the influence factors of ambient temperature, brightness, gender, dressing, fall posture, fall location, and scenario, a total of 640 tests are conducted and 5-fold cross validation is used to evaluate the classification performance. Experimental results indicate that the averages of the recall, precision, F1-Score, and detection accuracy are measured to be 91.25%, 94.76%, 92.97%, and 93.13%, respectively, which demonstrates that the proposed fall detection method is effective. Besides, the detection accuracy decreases from 96.88% to 85.94% as the ambient temperature rises. Hence, this noncontact fall detector can be widely applied for bedside fall detection at home, which is low cost, nonwearable, unobtrusive, noninvasive, and privacy preserved.**

***Index Terms*—Fall detection, feature extraction, image processing, infrared Sensor, radial basis function (RBF) neural network.**

Manuscript received 6 July 2022; revised 23 December 2022 and 25 January 2023; accepted 28 February 2023. Date of publication 3 March 2023; date of current version 7 July 2023. This work was supported in part by the National Natural Science Foundation of China under Grant 62104047, Grant U22A2012, Grant 62173098, and Grant U2001201. *(Corresponding authors: Heng Wu; Yangxing Wen.)*

Chunhua He, Shuibin Liu, Guangxiong Zhong, and Lianglun Cheng are with the School of Computer, Guangdong University of Technology, Guangzhou 510006, China (e-mail: hechunhua@pku.edu.cn; 2112205258@mail2.gdut.edu.cn; zhgx85@vip.qq.com; llcheng@gdut.edu.cn).

Heng Wu is with the School of Automation, Guangdong University of Technology, Guangzhou 510006, China (e-mail: heng.wu@foxmail.com).

Guizhen Yan is with the Institute of Microelectronics, Peking University, Beijing 100871, China (e-mail: gzyan@pku.edu.cn).

Yangxing Wen is with the Reproductive Medicine Center, The First Affiliated Hospital, Sun Yat-Sen University, Guangzhou 510080, China (e-mail: wenyx5@mail.sysu.edu.cn).

Digital Object Identifier 10.1109/JIOT.2023.3251980

I. Introduction

RECENTLY, population aging has been a global challenge faced by many countries in the world [1]. The population of the elderly (aged above 60) is predicted to reach 2.1 billion by 2050 [2]. The elderly aged above 65 are prone to fall, and the fall risk is about 28%–35%. For the elderly aged above 70, the fall risk increases to 32%–42% [3], [4]. The consequence induced by fall is very severe, such as bone fractures, head injuries and traumatic brain injuries. What is worse, unintentional falls may lead to death. Hence, fall detection and timely treatment are very important. The most common fall site for the elderly is on the bedside [5], therefore, this article will focus on the research of the detection method for beside fall. Nowadays, three kinds of fall detection methods, such as wearable device based, image based, and signs based, are prevalent [6], [7], [8].

Wearable device-based methods are often applied to fall detection, and MEMS inertial sensors are mostly adopted [9], [10]. For instance, inertial sensors are embedded in watches, belts, shoes or rings [11], [12], [13], [14], [15]. Fall events can be detected with the acquired activity data, and the detection precision is high. However, the shortages are that wearable devices may make the elderly uncomfortable, and the battery life is very short. What is worse, if they are shut down without power, the elderly will throw them aside.

Image-based methods mainly adopt RGB cameras, thermal cameras or depth cameras [16], [17], [18], [19], [20]. Background subtraction, barycenter calculation, moving speed of consequence frames, and the angle of body rotation are often used to extract the image features. Then, AI-based image processing algorithm is applied to identify the fall events. These noncontact detection techniques get rid of wearable discomfort, but the limitations are small field of view, high cost, and privacy invasion.

Signs-based methods often adopt WiFi modules, pressure sensors and millimeter-wave radar sensors [21], [22], [23], [24]. These sensors are often embedded in the bed, clothing, floor or ceiling. Based on the signal differences of vital-signs, fall events can be recognized. The bed-exit events can be detected accurately, however, the detection accuracy of bedside fall is not high. After all, there is no image for the human body recognition. Besides, in order to monitor the vital-signs signals accurately, the operation frequencies of the millimeter-wave radar sensors are often larger than 24 GHz, thus the devices'

prices are often very high. Although they are noninvasive, their installations are very complex.

Confronting the above limitations, some research institutes adopt low-resolution Infrared (IR) array sensors [25], [26]. They are noncontact, low cost, and privacy preserved. Whereas, if the number of IR pixels is not many enough, the resolutions will be low [27], [28], [29]. In order to advance the detection accuracy and protect the privacy, IR thermopile array sensor with 32 by 32 pixels can be adopted [30].

Pyroelectric infrared (PIR) sensors can be used to measure human's activities based on the infrared radiation changes (IRCs) [31]. Compared with thermal (IR) cameras and IR array sensors, the common point is that the detection principle is based on thermal radiation, but the difference is that the PIR sensors are used to monitor the human's activities, rather than human's thermogram. The advantages of the PIR sensors are low cost and high sensitivity to human's activities, which is conductive to fall recognition. However, owing to the lack of human's thermogram and image details, misjudgments are inevitable if PIR sensors are used alone. In order to improve the detection accuracy, multiple sensors, such as IR sensors, ultrasonic sensors, inertial sensors and depth sensors, can be combined together [32], [33], [34], [35], [36]. In addition, 5.8-GHz low-cost radar sensors can be also applied to measure human's activities. Compared with PIR sensors, the detection ranges are expanded and the still human body can also be detected. Moreover, the radar sensors can be fixed inside the plastic shell to advance the aesthetic feeling of the product.

In our previous work, the information of bed-exit and vital signs can be obtained by the sleep monitoring belt, but it cannot detect the bedside fall [37]. Considering that the consequences of bedside falls are very severe, this article will research the fall detection method for bedside application. A noncontact fall detection system based on the fusion of a low-resolution IR array sensor and a low-cost radar sensor will be proposed for the application in bedroom.

For fall detection with IR technique, preprocessing, feature extraction, and pattern recognition are often adopted [5], [6], [7]. Human positioning analysis is the key step of preprocessing, whereas, there are few reports about it. Statistical analysis, principal component analysis, spectrum analysis are common methods [38] for feature extraction to advance the detection accuracy. Finally, pattern recognition algorithms, such as random forest, support vector machine, K-nearest neighbor, logistic regression, convolutional neural network (CNN), and fuzzy clustering [39], [40], [41], [42], [43], are utilized to achieve the recognition. However, some of these algorithms are too complicated to be realized in the edge-computing processor. Given that cloud computing is not in time and unreliable, especially when the network is very unstable [44], [45], edge computing should be adopted. Thus, this article will present a simple bedside fall detection algorithm that can be easily realized in a local microprogrammed control unit (MCU).

II. System Design for Fall Detection

The system of a smart fall detector for bedside monitoring is composed of power supply subsystem, processor subsystem, and sensor subsystem.

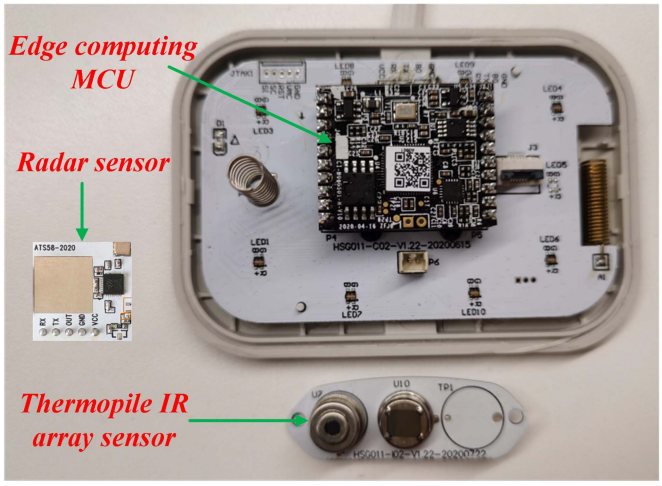

Fig. 1. Fall detection system based on a MEMS IR sensor and a radar sensor.

1) *Power Supply Subsystem:* The dc/dc converter, low dropout regulator and power adapter are applied to generate the appropriate supply voltages to the other subsystems.
2) *Processor Subsystem:* STM32F411 ARM is chosen as the edge-computing MCU. USB interface is used to connect with personal computer (PC), while the WiFi module is utilized to achieve the internet of Things (IoT) communication and remote fall alarm. A three-color LED indicator is used to display the detection result.
3) *Sensor Subsystem:* A radar sensor is used to detect the body movement, and it will output high level when somebody or body movement is detected. Otherwise, it will output low level. Thermopile IR array sensor is adopted to acquire the thermal image to judge whether there is a fall event happening at the bedside. Once a fall is detected, the indicator lights up in red.

The fall detection system based on a MEMS IR sensor and a radar sensor is illustrated in Fig. 1. The key components of the system are an edge computing MCU, a MEMS low-resolution thermopile IR array sensor, and a low-cost radar sensor.

ATS58-2020 is chosen as the radar sensor that is made by AirTouch (Shanghai) Intelligent Technology Company Ltd. It is a miniature 5.8-GHz radar sensor module whose size is about 20 × 20 mm. The core chip is AT5810S, which consists of a 5.8-GHz microwave circuit, an amplifier circuit, and a signal processor. Besides, a planar antenna is designed in the PCB and the detection area is illustrated in Fig. 2. TX pin is utilized to adjust the sensing distance, the sensing distance is 3∼5 m if TX is high level, while it can be advanced to 4∼6 m if TX is low level. Here, TX is set to high level. On the other hand, RX pin is utilized to tune the sensing delay. The sensing delay is 2 s when RX is high level, while it can be advanced to 30 s when RX is low level. Here, RX is set to high level. If somebody exits in the monitoring area of the radar, the sensor output SR is 1, otherwise, it is 0. The detection principle is that the feedback radar signal varies with heart beat and respiration, so the change of the feedback signal can be utilized to judge whether there is a person existing in the monitoring area.

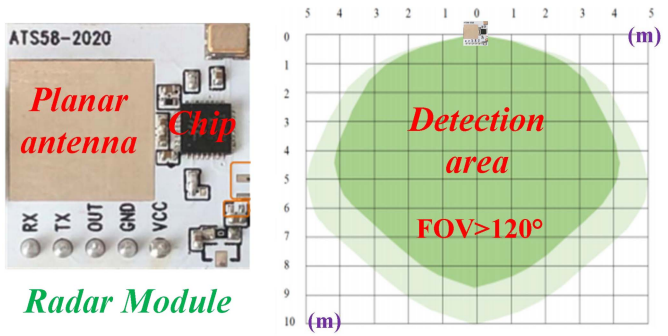

Fig. 2. Radar sensor module and its detection area.

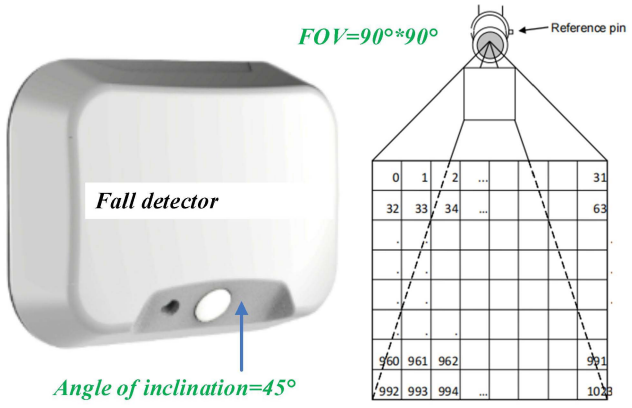

Fig. 3. Installation angle and FOV of the IR array sensor.

On the other hand, HTPA32x32dR2L2.1/0.8F5.0HiC is chosen as the thermopile IR array sensor, which is made by HEIMANN Sensor GmbH. Its resolution is 32 by 32 pixels, FOV is 90° by 90°, and the sampling frequency is up to 5 frames per second. Its accuracy is about $\pm 3\% * |To - Ta|$, where To and Ta stand for the objective temperature and ambient temperature, respectively. So, it is high precision and low cost. The fixed angle of inclination of the IR array sensor is 45°, thus the detector can better detect whether there is a fall in the area below the front, as shown in Fig. 3. The detector is mounted on the wall with double-sided adhesive tape. Obviously, the mounted scheme is different from those mentioned in the Introduction section, since most of the reported schemes is that the IR sensor is mounted on the ceiling.

For bedside application, the fixed height of the detector is set to 1.2 m. Generally, the upper surface of the mattress is 50-cm above the ground, thus the distance between the upper surface of the mattress and the detector is 70 cm. The detector is often installed beside the bed and aligned with the edge of the bed. If it is installed on the left side of the bed, the fall event on the left side of the bed is detected, and vice versa. In general, the elderly is easy to fall accidentally beside the bed, while children are easy to fall out of bed when they are asleep. For these cases, the detector is suitable and useful. According to the inclination angle and FOV, and considering the edge effect, the detection area (width by length) is about 1.2 m by 1.8 m, and it means that the effective fall detection area outside the bed is 0.6 m by 1.8 m, as illustrated in Fig. 4. As a matter of fact, the area of beside fall is often less than 0.6 m by 1.8 m, so the monitoring range of the detector is enough.

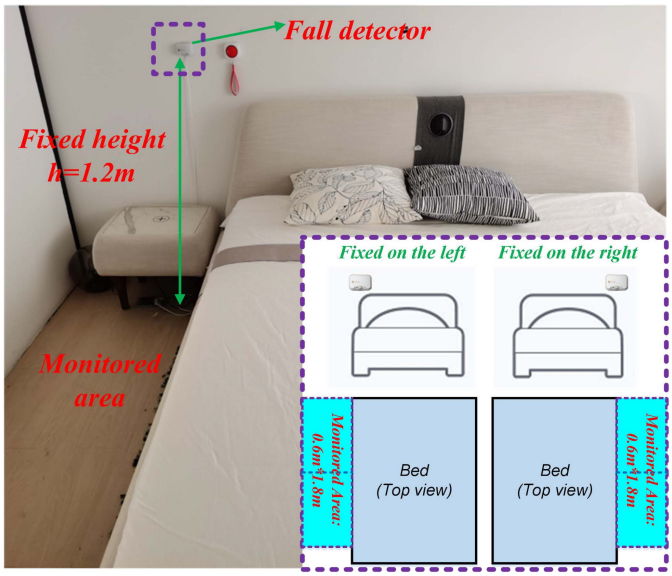

Fig. 4. Fixed height of the detector is 1.2 m and the effective fall monitored area is about 0.6 m by 1.8 m.

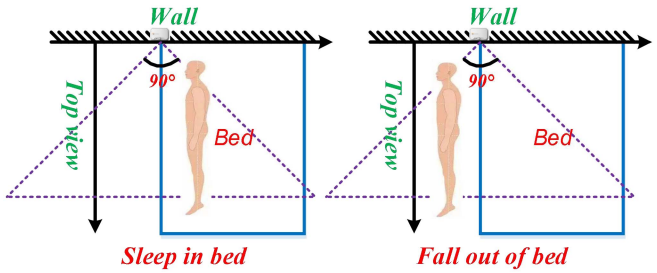

Fig. 5. Top view of someone sleeping in bed or falling out of bed.

For bedside application, the top view of someone sleeping in bed or falling out of bed is depicted in Fig. 5. Take the detector fixed on the left side of the bed as example, it is also obvious that the human body will appear on the right side of the thermal image before falling down. However, the body will appear on the left side of the thermal image after falling down. It means that the locked body area in the thermal image will shift to the left. Simultaneously, the locked body area will become slightly smaller as the distance increases. Therefore, the change of the locked body area in the thermal images can be used for fall detection. Compared with the detector mounted on the ceiling, the advantages of the detector mounted on the wall are as follows: 1) the detection resolution is larger; 2) the detector is easier to be installed; and 3) the detection principle is simpler.

In order to further advance the detection accuracy, combined with a radar sensor, this article will present a fusion diagnosis algorithm, which will be described in the next section. In addition, based on the test platform shown in Fig. 4, a series of fall experiments can be performed.

III. Fall Detection Method

The detection method for bedside fall mainly includes the algorithms of IR image processing, feature extraction, and pattern recognition.

A. IR Image Processing Algorithm

IR image processing is composed of noise suppressing, block processing, and body area locking.

1) Noise Suppressing: The MEMS IR array sensor outputs 32 by 32 pixels absolute temperature distribution via I^2C bus at maximum 5 frames per second. That is, there are 1024 objective temperature values and an ambient temperature value, and the maximum sampling rate f_s is 5 Hz. Because the temperature signal is apt to be disturbed by the ambient noise, it is necessary to filter the noise before thermal image recognition.

The noise of IR temperature signal is usually nonstationary, that is, its statistical characteristics may change with time. The adaptive filtering does not need to know or estimate the statistical characteristics of the analyzed signal, but directly uses the signal observation value and recursively updates the parameters in the observation process according to a certain criterion, so as to gradually approaches an optimal processing result. Thus, adaptive filter is adopted in this article.

Assume that $\boldsymbol{X(k)}$ is an observation vector, and $\boldsymbol{W(k)}$ is a weight vector, then the output of the filter $y(k)$ is defined as

$$y(k) = W^T(k)X(k) \tag{1}$$

where k is the sampling index. If $d(k)$ is the expected output, then the predicted error e(k) is derived as

$$e(k) = d(k) - y(k) = d(k) - W^T(k)X(k). \tag{2}$$

Thus, according to steepest descent method, the recurrence formula of the weight vector is deduced as

$$W(k+1) = W(k) + 2\mu \mathrm{e}(k)X(k) \tag{3}$$

where μ is a step factor. The larger the step factor is, the faster the convergence speed is, the worse the filtering effect is, and vice versa. Here, it is set to 0.1. From (1)–(3), we can see that adaptive filter is easy to be realized. Considering that there are 1025 temperature signals should be processed by the adaptive filter, in order to reduce the calculation amount, the equations of adaptive filtering can be further simplified. Now that the temperature signal is a slowly varying signal, $\boldsymbol{X(k)}$ can be regarded as a constant vector, such as a unit vector. Considering a special case, there is only one parameter in $\boldsymbol{X(k)}$ and $\boldsymbol{W(k)}$, that is, the two vectors degenerate into two scalars, then the equations above can be deduced as

$$y(k) = W(k) \tag{4}$$

$$e(k) = d(k) - y(k) = d(k) - W(k) \tag{5}$$

$$W(k+1) = W(k) + 2\mu \mathrm{e}(k) = W(k) + 2\mu[d(k) - W(k)]. \tag{6}$$

Thus, the transfer function in the discrete frequency domain (z domain) can be derived as

$$\frac{Y[z]}{D[z]} = \frac{2\mu z}{z + (2\mu - 1)} \tag{7}$$

where D and Y is the z-transform results of the time domain signals d and y, respectively. After bilinear transformation with (8), the transfer function in the time domain (s domain) can be derived as (9)

$$z = \frac{2f_s + s}{2f_s - s} \tag{8}$$

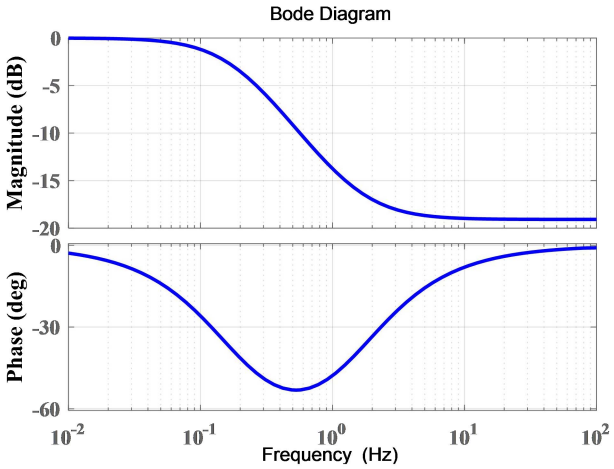

Fig. 6. Bode diagram of the adaptive filter.

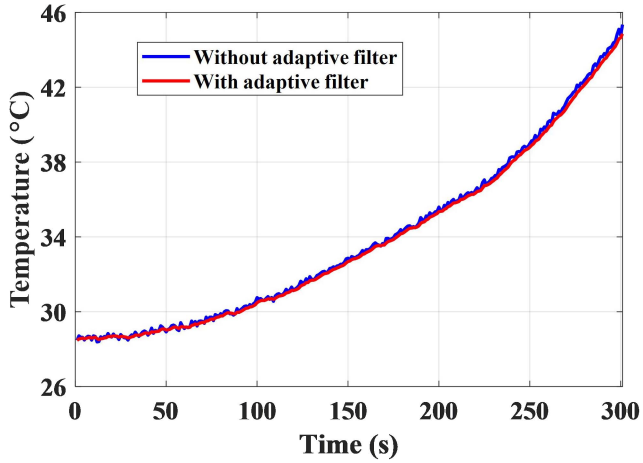

Fig. 7. Fluctuation of the temperature signal is suppressed by the adaptive filter.

$$\frac{Y[s]}{D[s]} = \frac{\mu}{1-\mu}\frac{s + 2f_s}{s + 2\mu f_s/(1-\mu)}. \tag{9}$$

Because μ is set to 0.1, the transfer function shown in (9) can be regarded as a first-order low pass filter (LPF), and the bode diagram is shown in Fig. 6. The high-frequency noise can be suppressed by this filter, and the fluctuation of the measured signal is indeed reduced, as shown in Fig. 7. Therefore, this filter is effective. After filtered, the thermal image of 32*32 temperature points is illustrated in Fig. 8, and the colors of these points are determined by their values. Generally, red and green represent high and low temperature, respectively.

2) Block Processing: The temperature of the human body is usually higher than the background temperature. Thereby, in order to identify the body area, the high-temperature points should be marked first. Simultaneously, in order to remove the influence induced by extremely high or low temperature points, the temperature points higher than 40 °C or lower than 0 °C will be eliminated, then the maximum and minimum of the remaining temperature points can be calculated as $T_{\max}$ and $T_{\min}$, respectively.

First, the temperature threshold T_{thk} at the kth moment should be confirmed, which will be applied to distinguish the high temperature points from the low temperature points. Here, successive approximation algorithm is adopted, as follows.

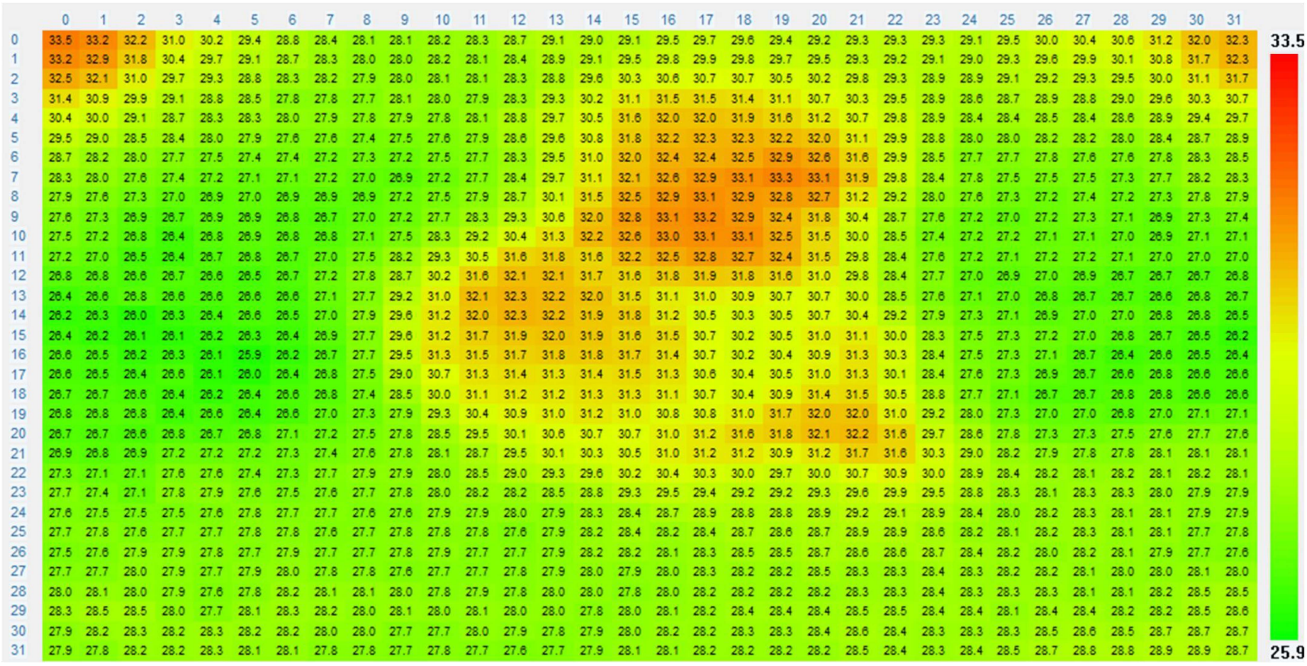

Fig. 8. Thermal image of 32*32 temperature points of the IR array sensor.

1) At the beginning, the average of $T_{\max}$ and $T_{\min}$ is calculated and assigned to T_{mm}, as shown in

$$T_{mm} = (T_{\max} + T_{\min})/2. \tag{10}$$

2) T_{thk} is set to T_{mm}, and compute the average *TM1* of the temperature values that are larger than T_{thk} and smaller than $T_{\max}$. Similarly, compute the average *TM2* of the temperature values that are larger than $T_{\min}$ and smaller than T_{thk}. Afterward, update T_{mm} with the average of *TM1* and *TM2*. At this time, if the absolute value of $(T_{mm} - T_{thk})$ is less than 0.5 °C, step 3 will be performed, otherwise, step 2 is repeated. The pseudocode is shown as (11), where sum1, sum2, *cnt1*, and *cnt2* are four variables used to calculate the averages. Here, assume that $\boldsymbol{T}$ is the current IR temperature array, whose size is 32*32. r is the row index ($1 \le r \le 32$) and c is the column index ($1 \le c \le 32$)

```
while(1)
{T_thk = T_mm;  sum1 = cnt1 = sum2 = cnt2 = 0;
 for r = 1:32
 for c = 1:32
 { if T[r][c] ∈ [T_thk, T_max]
  {sum1 = sum1 + T[r][c];  cnt1 + +; }
   else if T[r][c] ∈ [T_min, T_thk)
  {sum2 = sum2 + T[r][c];  cnt2 + +; }
 }
 TM1 = sum1/cnt1; TM2 = sum2/cnt2;
 T_mm = (TM1 + TM2)/2;
 if(|T_mm − T_thk| < 0.5) break;
}
```
(11)

3) If step 2 is stop, T_{thk} is confirmed, which equals to T_{mm}, as shown in the following:

$$T_{thk} = T_{mm}. \tag{12}$$

Hence, the high temperature points larger than T_{thk} and smaller than $T_{\max}$ can be picked out, and marked with a block number larger than 0. Here, the double boundary scans algorithm is used for block processing, which consists of three steps as follows.

1) *First Boundary Scan:* Define $\boldsymbol{M}$ as a label array, and the initial values of the elements in $\boldsymbol{M}$ are all 0. Here, boundary extension and progressive scanning are adopted, and the size of $\boldsymbol{M}$ is 34*34. Meanwhile, define *bn* as a block number, whose initial value is 1. Thus, for r ($1 \le r \le 32$) and c ($1 \le c \le 32$), a new data set ***S1*** can be obtained as {$\boldsymbol{M}[r-1][c-1]$, $\boldsymbol{M}[r-1][c]$, $\boldsymbol{M}[r-1][c+1]$, $\boldsymbol{M}[r][c-1]$, $\boldsymbol{M}[r][c+1]$, $\boldsymbol{M}[r+1][c-1]$, $\boldsymbol{M}[r+1][c]$, $\boldsymbol{M}[r+1][c+1]$}. Afterward, "0" and the repeated value in set ***S1*** are eliminated to form set ***S2***. If ***S2*** is an empty set, *bn* is assigned to $\boldsymbol{M}[r][c]$, and then updated as $(bn+1)$. Otherwise, the minimum in ***S2*** will be assigned to $\boldsymbol{M}[r][c]$. Meanwhile, if the size of ***S2*** is larger than 1, it means that these blocks are connected together, then ***S2*** will be added to the relationship table $\boldsymbol{R}$ whose initial value is empty. Thus, $\boldsymbol{R}$ is composed of a series of sets. Here, the pseudo code is shown as

```
bn = 1;  i = 1;  R = ∅;
for r = 1:32
for c = 1:32
 if T[r][c] ∈ [T_th, T_max]
 { if(S2 == ∅)
    {M[r][c] = bn;  bn = bn + 1; }
```

$$\begin{aligned}&\text{else}\\&\{M[r][c] = \min(S2);\\&\text{if(size}(S2) > 1)\ \text{R}[i++] = S2;\ \}\\&\}.\end{aligned} \tag{13}$$

2) *Second Boundary Scan:* After the first boundary scan, there may be some adjacent points marked with different block numbers, as shown in Fig. 9, blocks 3–5 are connected together. In fact, these adjacent blocks should be combined together and they belong to the same block. Hence, the second boundary scan is applied to deal with the relationship table $\boldsymbol{R}$. First, compare all the elements in $\boldsymbol{R}$, if the intersection of any two elements is not empty, then merge them to form a union. Second, for each element in $\boldsymbol{R}$, pick out the points corresponding to all block numbers in the same set, and then change their labels to the minimum block number of the set. In this way, after every element in $\boldsymbol{R}$ is processed, the adjacent blocks are merged together. As shown in Fig. 10, blocks 3–5 are merged together, and the final block number is 3. The pseudo code is shown as (14), where the counter array ***cnt*** is used to record the number of the points in each block, whose initial value is 0

$$\begin{aligned}&\text{for } i = 1{:}\text{size}(R)\\&\text{for } j = (i+1)\ :\ \text{size}(R)\\&\ \text{if}(R[i] \bigcap R[j] \neq \varnothing)\\&\ \ \{R[i] = R[i] \bigcup R[j];\ \ R[j] = \varnothing;\ \}\\&\text{for } r = 1{:}32\\&\text{for } c = 1{:}32\\&\text{for } i = 1{:}\text{size}(R)\\&\ \text{if}(M[r][c] \in R[i])\\&\ \{M[r][c] = \min(R[i]);\\&\ \ cnt[\min(R[i])] + +;\}\end{aligned} \tag{14}$$

3) Due to the influence of the environment, perhaps several high-temperature blocks are identified, and the area of the block corresponding to the human body is often the largest. Besides, the number of the locked points of the human body is generally larger than 15; hence, some noise blocks can be eliminated by the area analysis, as shown in (15), where id is the index (i.e., block number) of the largest block. Finally, only the blocks with larger area are reserved, and other identified blocks will be removed. As shown in Fig. 11, we can see that blocks 1, 2, and 6 have been removed, and only block 3 is reserved. Due to the influence of background or other factors, there may be some unlocked points within the contour line of the high temperature block. As shown in Fig. 11, these singular points (i.e., noise points) must be filtered out, because the locked human contour should not contain some unlocked points theoretically. Therefore, mathematical morphology processing will be adopted to achieve the goal

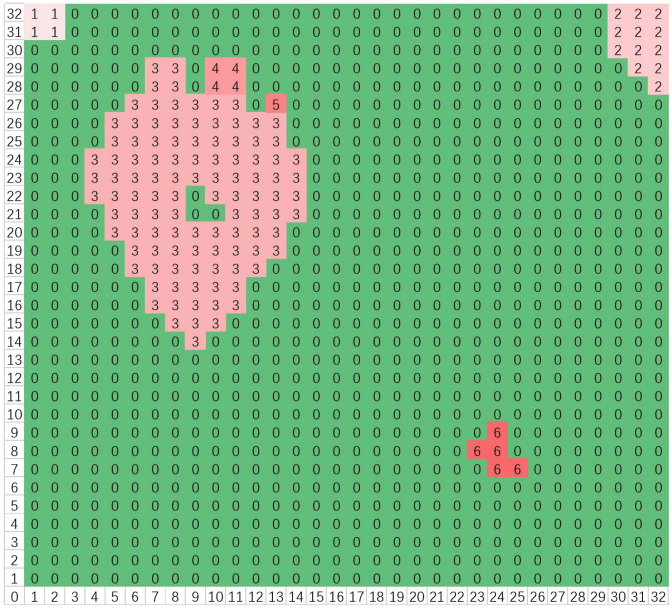

Fig. 9. Results of the first boundary scan: every point is marked with block number according to the temperature value.

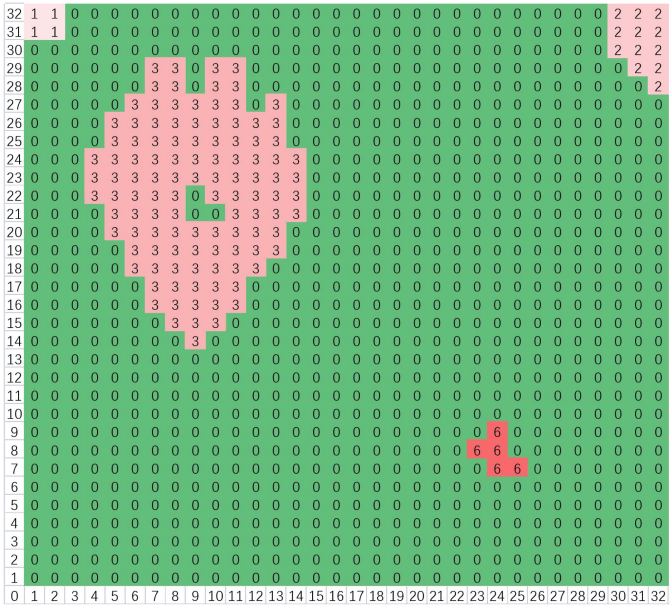

Fig. 10. Results of the second boundary scan: the adjacent blocks are merged together.

$$\begin{aligned}&\text{id} = \text{find}(\max(cnt));\\&\text{for } r = 1{:}32\\&\text{for } c = 1{:}32\\&\{\ \text{if}(cnt[M[r][c]] \leq 15)\ M[r][c] = 0;\}\end{aligned} \tag{15}$$

3) Body Area Locking: Binary mathematical morphology processing includes erosion, dilation, opening and closing operations. Here, dilation operation is defined as (17), it means that if the label of a certain point is *ide* (*ide* > 0), then the labels of its adjacent eight points should be set as *ide*. Similarly, erosion operation is defined as (17), it means that if the minimum of the labels corresponding to the adjacent 8 points is 0, or the point is at the extended boundary, then the label of this point

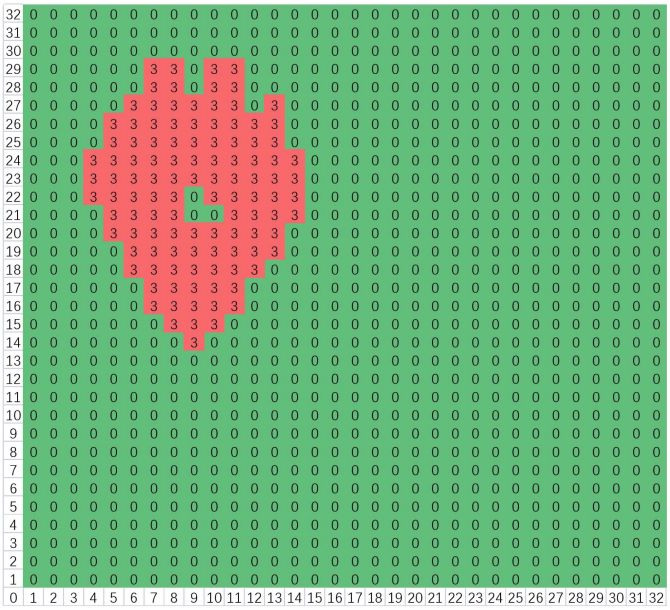

Fig. 11. Blocks with larger area are reserved, and the other noise blocks are all removed.

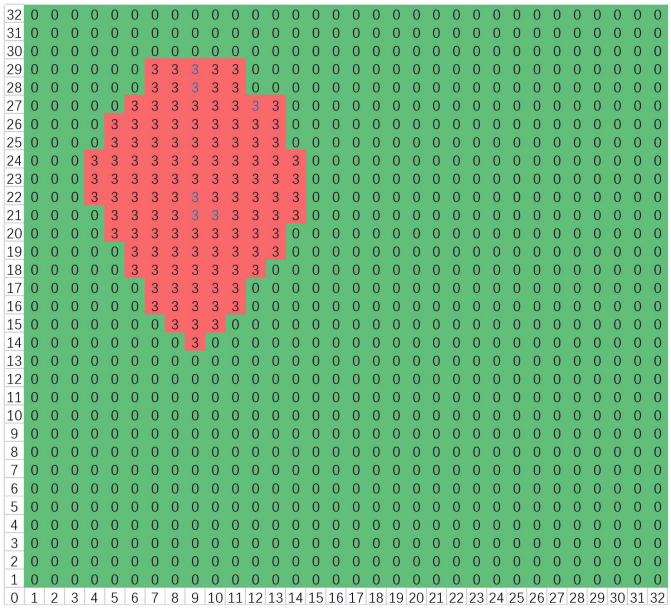

Fig. 12. Negative noise is filtered by a closing operation, and the six new locked points are dyed blue.

should be set as 0. In (17) and (17), ***M'*** is an array variable, whose size is 34*34

$$
\begin{aligned}
&\text{for } r = 1{:}32\\
&\text{for } c = 1{:}32\\
&\ \text{if}(M[r][c] == ide)\\
&\ \{M'[r-1][c-1] = M'[r-1][c] = M'[r-1][c+1] = ide;\\
&\ \ M'[r][c-1] = M'[r][c] = M'[r][c+1] = ide;\\
&\ \ M'[r+1][c-1] = M'[r+1][c] = M'[r+1][c+1] = ide;\\
&\ \}\\
&\text{for } r = 0{:}33\\
&\text{for } c = 0{:}33\\
&\ \{M[r][c] = M'[r][c];\ \}
\end{aligned}
\tag{16}
$$

$$
\begin{aligned}
&for\ r = 0{:}33\\
&\text{for } c = 0{:}33\\
&\{\ \text{if}((r == 0)||(r == 33)||(c == 0)||(c == 33))\ M'[r][c] = 0;\\
&\ \ \text{else if}(\min(S1) == 0)\ M'[r][c] = 0;\\
&\ \ \text{else } M'[r][c] = M[r][c];\\
&\ \}\\
&\text{for } r = 0{:}33\\
&\text{for } c = 0{:}33\\
&\ \{M[r][c] = M'[r][c];\}
\end{aligned}
\tag{17}
$$

Closing operation will first perform dilation operation, then perform erosion operation, which can filter the negative impulse noise in the image. On the contrary, opening operation will first perform erosion operation, then perform dilation operation, which can filter the positive impulse noise in the image. Therefore, in order to remove the negative and positive noises simultaneously, closing operation and opening operation are cascaded. As shown in Fig. 12, the negative noise is filtered by a closing operation, and the six new locked points are dyed blue. Subsequently, the positive noise is filtered by an opening operation, and the removed point is also dyed blue, as shown in Fig. 13. These results figure out that the binary mathematical morphology processing is indeed effective to filter the noises in the 2-D image. If a locked potential body area appears after IR image processing, then feature extraction will be conducted.

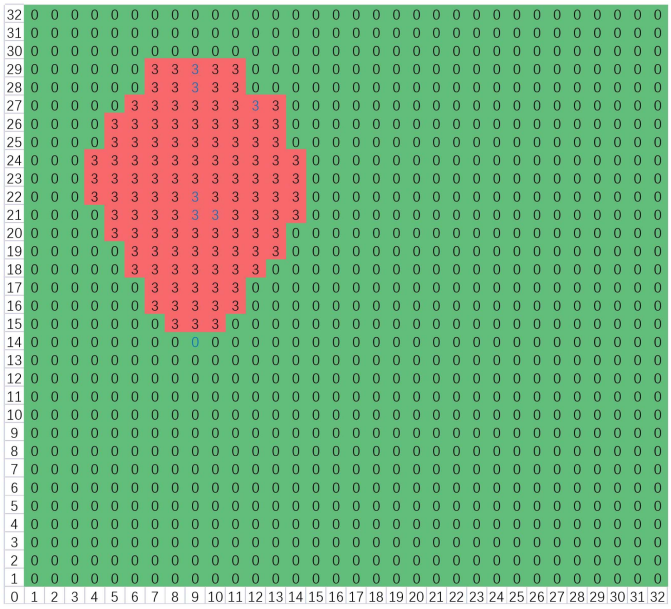

Fig. 13. Positive noise is filtered by an opening operation, and the removed point is also dyed blue.

B. Feature Extraction Algorithm

In this article, bedside fall refers to somebody falls from the bed, and cannot get up but lying on the ground beside the bed. Given that the fall events have something to do with time and

space, so the related features should be extracted, and partition processing algorithm is adopted here.

Since the fall detector is installed beside the bed and aligned with the edge of the bed, as shown in Fig. 4, the center line of the IR image will be aligned with the edge of the bed. Take the center line as the dividing line, the thermal image can be divided into two parts. The part monitoring the bed is Part A, while the other part is Part B. Assume that there are k high-temperature blocks identified by double boundary scans algorithm, and sorted by area from large to small, they are named *BL1*, *BL2*, …, *BLk*. Thus, the corresponding numbers of the locked points of them are *NL1*, *NL2*, …, *NLk*, and *NL1* $\geq$ *NL2* $\geq$ … $\geq$ *NLk*. Besides, the points of the *kth* locked high-temperature block may be located in Part A or Part B. Therefore, block *BLk* can be divided into *BLk_A* and *BLk_B*, and the corresponding numbers of locked points are marked as *NLk_A* and *NLk_B*, respectively. Here, *NLk* = *NLk_A* + *NLk_B*.

First, define *BL_A* and *BL_B* as two block variables, whose corresponding numbers of the locked points are *NL_A* and *NL_B*, respectively. The corresponding mean temperatures of the two blocks are defined as $T_{cA}$and T_{cB}, respectively. Besides, the center coordinate (X_{cA}, Y_{cA}) of block *BL_A* can be obtained by averaging the abscissas and ordinates of all the points in the locked area. The difference of the center coordinates at adjacent moments is calculated as (dX_{cA}, dY_{cA}). Thereby, the standard deviation of the latest 5 center coordinates can be obtained as $(stdX_{cA}, stdY_{cA})$. That is, the statistical analysis is performed with the data in the latest 1 s because f_s is 5 Hz. If $stdX_{cA}$ and $stdY_{cA}$ are both less than 1, and the absolute values of dX_{cA} and dY_{cA} are both smaller than 2, it indicates that the locked body area is stable, and the corresponding moment is called stable moment. Then, the stable center coordinate $(\mathrm{SX}_{cA}, \mathrm{SY}_{cA})$ of the locked area can be updated by averaging the latest 5 center coordinates. If the locked body area in Part A is stable, *flag_stableA* is set to 1, otherwise it is set to 0 and $(\mathrm{SX}_{cA}, \mathrm{SY}_{cA})$ will be not updated, as shown in (18). Likewise, the definitions of (X_{cB}, Y_{cB}), (dX_{cB}, dY_{cB}), $(stdX_{cB}, stdY_{cB})$, $(\mathrm{SX}_{cB}, \mathrm{SY}_{cB})$, flag_stableB in Part B are similar to those in Part A

$$\begin{aligned}&\text{if}((stdX_{cA} < 1)\&\&(stdY_{cA} < 1)\&\&(|dX_{cA}| < 2)\&\&(|dY_{cA}| < 2))\\&\quad \text{flag\_stableA} = 1;\\&\text{else flag\_stableA} = 0.\end{aligned} \tag{18}$$

There are three steps to confirm whether there is a fall action. In the first step, *BL1_A* and *NL1_A* are assigned to *BL_A* and *NL_A*, respectively. If condition (19) is met, flag_*A* will be set to 1 and jump to the second step, otherwise, the judgment is repeated

$$\begin{aligned}&BL\_A = BL1\_A;\ \ NL\_A = NL1\_A;\\&\text{if}((\text{flag\_stableA} == 1)\&\&(NL\_A > NL1 * 0.8)\\&\quad \&\&(15 < NL\_A < 200)\&\&(1 < \mathrm{SX}_{cA} < 30))\\&\quad \text{flag\_}A = 1.\end{aligned} \tag{19}$$

It means that if there is a person in Part A, *NL_A* should be larger than 0.8**NL1_A* and 15, and smaller than 200. Besides, the stable center cannot be close to the boundary, hence SX_{cA} should be larger than 1 and smaller than 30. If flag_*A* equals 1, the corresponding parameters *BL_A*, SX_{cA}, SY_{cA}, *NL_A,* T_{cA}, and $\boldsymbol{T}$ are assigned to *BL_A0*, SX_{cA0}, SY_{cA0}, *NL_A0*, T_{cA0}, and $\boldsymbol{T_0}$, respectively. The changes of the temperatures of the new locked area can be evaluated by the Euclidean Distance (ED), as shown in

$$\begin{aligned}&\text{ED} = 0;\\&\text{for } r = 1{:}32\\&\text{for } c = 1{:}32\\&\{\ \text{if}(M[r][c] == \text{id})\\&\quad \text{ED} = \text{ED} + (T[r][c] - T_0[r][c])^2;\\&\quad \}\\&\quad \text{ED} = \sqrt{\text{ED}}.\end{aligned} \tag{20}$$

In the second step, *BL_B* is the maximum block in Part B. If the condition (21) is met, flag_*B* will be set to 1 and jump to the third step, otherwise, the judgment is repeated

$$\begin{aligned}&BL\_B = \max(BL1\_B, BL2\_B, \ldots, BLk\_B);\\&NL\_B = \max(NL1\_B, NL2\_B, \ldots, NLk\_B);\\&\text{if}((|T_{cB} - T_{cA0}| < 2)\&\&(0.5 < \frac{NL\_B}{NL\_A0} < 1)\\&\quad \&\&(15 < NL\_B < 200)\&\&(\text{ED} > 10)\&\&(\text{SR} == 1)\\&\quad \&\&(|\mathrm{SX}_{cB} - \mathrm{SX}_{cA0}| > \text{LX})\&\&(|\mathrm{SY}_{cB} - \mathrm{SY}_{cA0}| < \text{LY})\\&\quad \&\&(1 < \mathrm{SX}_{cB} < 30)\&\&(\text{flag\_stableB} == 1))\\&\quad \text{flag\_}B = 1\end{aligned} \tag{21}$$

where LX and LY are the current span of the locked area in the x-axis direction and y-axis direction, respectively. In General, there is a large displacement in the x-axis direction after falling, while the displacement in the y-axis direction is relatively small. Hence, if somebody falls from the bed, the displacement in the y-axis direction should be less than LY, while it should be larger than LX in the x-axis direction. Besides, the stable center cannot be close to the boundary, hence SX_{cB} should be larger than 1 and smaller than 30. The difference of the mean temperatures of the locked area before and after falling down should be smaller than 2 °C. The ratio of the locked area after falling down to the locked area before falling down should be larger than 0.5 and less than 1, as illustrated in Fig. 14. Meanwhile, *NL_B* should be larger than 15 and smaller than 200, since the body's area is limited. In order to eliminate the influence of other existed heat sources, ED should be larger than 10. If *ED* is small, it means that the new locked area has already existed before falling down, and it is an unreasonable fall change. If somebody exists in the monitoring area of the radar, the sensor output SR is 1, otherwise, it is 0. As shown in Fig. 14, the locked body area moves to the right after falling down. However, there may be a residual thermal block left on the left. Therefore, next step is very necessary to eliminate the influence resulted from the residual temperature on the bed.

In the third step, go back to analysis the high-temperature block with maximum area (i.e., *BL_A*) in Part A after falling down, if the condition (22) is met, flag_action will be set to

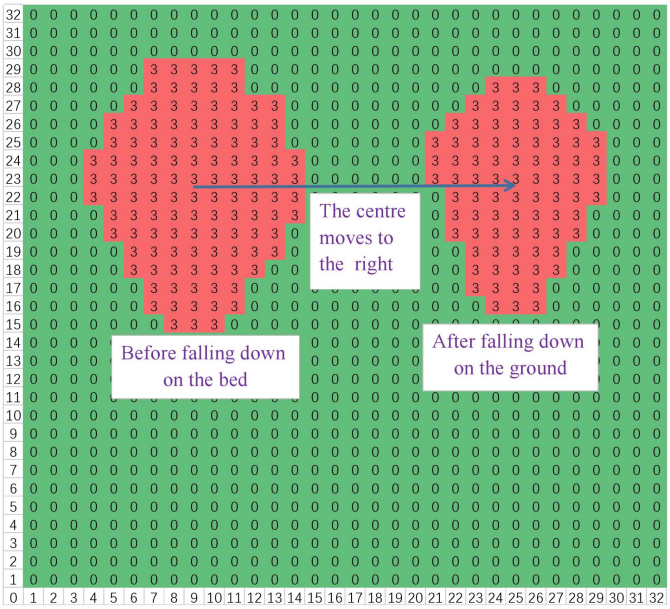

Fig. 14. Locked body area moves to the right after falling down.

1, and pattern recognition for fall detection will be conducted

$$\begin{aligned} &BL\_A = \max(BL1\_A, BL2\_A, \ldots, BLk\_A);\\ &NL\_A = \max(NL1\_A, NL2\_A, \ldots, NLk\_A);\\ &\text{if}(BL\_A \bigcap BL\_A0 \neq \varnothing)\\ &\{\text{if}((\text{flag\_}B == 1)\&\&(\frac{NL\_A}{NL\_A0} < 0.5))\\ &\quad \text{flag\_action} = 1;\}\\ &\text{else flag\_action} = 1 \end{aligned} \tag{22}$$

where if the intersection of block *BL_A0* and block *BL_A* is empty, then flag_action is set 1 directly; Otherwise, if flag_*B* is equal to 1, and the ratio of *NL_A* to *NL_A0* is smaller than 0.5, then flag_action is also set 1. It means that the previous locked area in Part A is decreasing because the residual temperature on the bed is gradually dissipated after human body falls, and its influence is eliminated. Similarly, the influences induced by ambient thermal noise and the other persons can be suppressed by these operations. Therefore, it is very important to analyze the dynamic changes of the old and new thermal images.

At the initial moment when flag_action becomes 1, the corresponding T_{cB} and *NL_B* are recorded as T_{cB0} and *NL_B0*. Once flag_action and flag_stableB are both equal to 1, start a timer to record the duration t_d, meanwhile, monitor the human activity based on the radar sensor, and count the time t_{ac} of body movement within the latest 1 min. Hence, if the condition (23) is met, the fall action disappears, and flag_action, flag_*A*, and flag_*B* will be set to 0

$$\begin{aligned} &\text{if}((|dX_{cB}| > 2)||(|dY_{cB}| > 2)||(t_d > 120)\\ &\quad ||(|T_{cB} - T_{cB0}| > 2)||(|NL\_B - NL\_B0| > NL\_B0/3))\\ &\qquad \text{flag\_action} = \text{flag\_}A = \text{flag\_}B = 0. \end{aligned} \tag{23}$$

That is, if the locked body area in Part B is unstable (e.g., the displacement of the center is larger than 2), or the duration t_d is longer than 120 s, or the change of the mean temperature

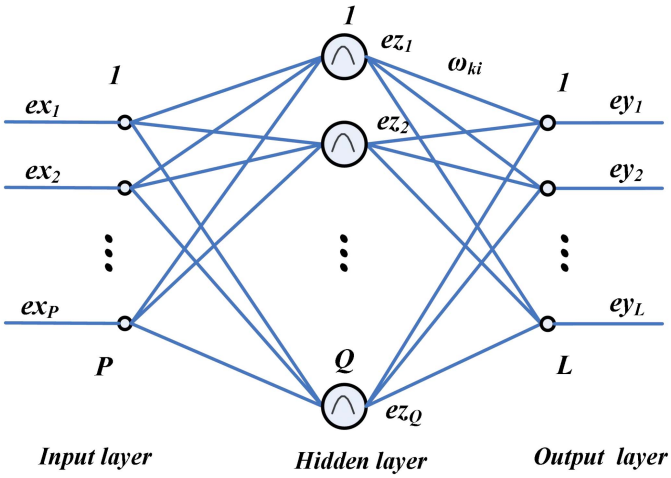

Fig. 15. Architecture of a three-layer RBF neural network system.

of the locked area is larger than 2 °C, or the locked area changes by more than 1/3, then the states of flag_action, flag_*A* and flag_*B* should be restored. Obviously, these constraints are applied to suppress the influence of residual or existed heat sources on the bed or ground.

In general, if the body activities are more after the thermal image moves out of bed, it means that the objective may struggle to get up after falling down or do other things, so there is no need to alarm in these cases. Only when the thermal image is basically stable after moving out of bed, and the body activities are less within 1 min, can it be recognized as a fall. In addition, body activity detection can reduce the influence of abnormal interferences induced by sunlight, light, bedside company, etc. Therefore, a radar sensor is introduced in this article to assist in the fall judgment, which is very significant to further reduce the misjudgment.

Assume that std*NL_B* and $stdT_{cB}$ are the standard deviations of *NL_B* and T_{cB} within 1 s, respectively. Given that $stdX_{cB}$, $stdY_{cB}$, *stdNL_B*, $stdT_{cB}$, t_d, t_{ac}, flag_stableB, and flag_action are closely related to the fall event, hence, these eight parameters will be used as the inputs for pattern recognition. Once the fall action is detected and recognized, fall event analysis will be initiated.

C. Pattern Recognition Algorithm

Neutral network algorithm is widely used for prediction control, system identification, fitting, classification, and pattern recognition. In this article, a three-layer radial basis function (RBF) neural network algorithm is utilized for the pattern recognition, as shown in Fig. 15, where $\mathbf{EX}=(ex_1, ex_2, \ldots, ex_P)^T$ is the input matrix of input layer, $\mathbf{EZ}=(ez_1, ez_2, \ldots, ez_Q)^T$ is the output matrix of hidden layer, and $\mathbf{EY} = (ey_1, ey_2, \ldots, ey_L)^T$ is the output matrix of output layer. The numbers of the neurons of input layer, hidden layer and output layer are *P*, *Q*, and *L*, respectively. Gaussian function is continuous derivable, so it is adopted as the transfer function of the hidden layer, as depicted in

$$ez_i = \exp\left[-\frac{(\mathrm{EX} - C_i)^T(\mathrm{EX} - C_i)}{2\delta_i^2}\right],\ i = 1, 2, \ldots, Q \tag{24}$$

where ez_i is the ith output of the hidden layer, and δ_i is a normalization constant of the ith hidden-layer node. $\boldsymbol{C_i}$ is the center vector of the ith hidden-layer node, whose dimension is the same as that of **EX**. ez_i is between 0 and 1, which reaches maximum when **EX** equals $\boldsymbol{C_i}$. Linear function is adopted as the transfer function of the output layer, as shown in

$$ey_k = \sum_{i=1}^{Q} \omega_{ki} ez_i - b_k, \ \ k = 1, 2, \ldots, L \tag{25}$$

where ey_k is the kth output, ω_{ki} and b_k are the weight factor and threshold of the output layer, respectively. It is not until the training error (TE) satisfies the setting target that the training stops, then all the parameters of the network are confirmed. The calculation formula of TE is defined as

$$\mathrm{TE} = (\mathrm{EY} - \mathrm{TT})^T \times (\mathrm{EY} - \mathrm{TT})/2 \tag{26}$$

where **TT** is the expected output. In general, the training includes unsupervised learning period and supervised learning period. After training, the network can be utilized for online fall recognition.

In this article, **EX** is [$stdX_{cB}$, $stdY_{cB}$, $stdNL\_B$, $stdT_{cB}$, t_d, t_{ac}, flag_stableB, flag_action], and **EY** is [fall or nonfall]. Hence, P is 8 and L is 1. In order to advance the learning effect, Q is set to 24. In the leaning process, the learning rate is set to 10^{-4} and the maximum epoch is set to 1000. In fact, the learning process can be fulfilled in the computer to save the time, after the parameters are confirmed, the network will be applied to the recognition in the MCU. The architecture of this RBF neural network is so simple that it can be easily realized in the MCU. Therefore, the edge computing is feasible.

IV. Experimental Results

Since the fall detector is an IoT product, the test results can be also obtained by the APP in a smartphone. In order to evaluate the performances of the proposed detection method, the precision (PR), recall (RE), F1-Score, and recognition accuracy (ACC) are defined as

$$\begin{aligned} \mathrm{PR} &= \frac{\mathrm{TP}}{\mathrm{TP}+\mathrm{FP}}, \ \ \mathrm{RE} = \frac{\mathrm{TP}}{\mathrm{TP}+\mathrm{FN}} \\ F_1 - \mathrm{Score} &= \frac{2 \times \mathrm{RE} \times \mathrm{PR}}{\mathrm{RE}+\mathrm{PR}} \\ \mathrm{ACC} &= \frac{\mathrm{TP}+\mathrm{TN}}{\mathrm{TP}+\mathrm{TN}+\mathrm{FP}+\mathrm{FN}} \end{aligned} \tag{27}$$

where TP (True Positive) is the number of correctly detected abnormal epochs (i.e., fall), TN (True Negative) is the number of correctly detected normal epochs (i.e., nonfall), FP (False Positive) is the number of incorrectly detected normal epochs (i.e., nonfall), and FN (False Negative) is the number of incorrectly detected abnormal epochs (i.e., fall). Hence, these 4 parameters are the most important performance indexes.

A. Test Scheme Design

Several main influence factors for bedside fall are shown in Table I, namely, ambient temperature, brightness, gender, dressing, fall posture, fall location and scenario. Except that ambient temperature has five levels, other factors have only two levels. Given that ambient temperature is the most important influence factor, it will be set to 18 °C, 21 °C, 24 °C, 27 °C, and 30 °C, respectively. It can be controlled by an air conditioner that can heat or cool. The experimental site is shown in Fig. 4, and a series of bedside fall tests (i.e., imitate that somebody falls from the bed or gets out of bed normally) will be conducted.

TABLE I
Several Main Influence Factors for Bedside Fall Tests

Factor	Level
Ambient temperature	18°C, 21°C, 24°C, 27°C, 30°C
Brightness	sunlight, LED light
Gender	male (1.8m), female (1.6m)
Dressing	thin clothes, thick clothes
Fall posture	lying, sitting
Fall location	in the center, at the boundary
Scenario	quilt cover, no quilt cover

Moreover, brightness is another key influence factor, which is mainly adjusted by sunlight or LED light. As for gender and height, a young man with a height of 1.8 m and a young woman with a height of 1.6 m are recruited to imitate the bedside falls or nonfalls of the elderly. The fall posture is often lying or sitting on the ground, while the fall location is often in the center or at the boundary. In addition, during the sleeping, the elderly may dress the thin or thick clothes, and cover a quilt or not. Hence, considering the fall or nonfall situation, for every ambient temperature, there are 128 (=2^7) tests in total. Thus, a total of 640 (=128 * 5) tests will be conducted.

B. Test Results

In this article, 5-fold cross validation is applied to evaluate the classification performance. Given that ambient temperature is the most important influence factor, the test data are divided into five groups according to the setting ambient temperature, and each group has 128 pieces of data corresponding to 128 tests. Here, assume that G1, G2, G3, G4, and G5 represent the data set of 18 °C, 21 °C, 24 °C, 27 °C, 30 °C, respectively. For each fold, four data sets are applied for training while the rest one is used for validation. For example, for Fold No.1, {G2, G3, G4, G5} are utilized for training and G1 is applied for validation. Similarly, for Fold No.2, No.3, No.4, and No.5, data set G2, G3, G4, and G5 are used for validation, respectively. Thus, 80% of the data are used for training while 20% of the data are used for validation.

The test results of TP, TN, FP, FN of 5-fold cross validation are listed in Table II, then RE, PR, F1-Score, and ACC of them are calculated according to (27), as depicted in Fig. 16. The averages of TP, TN, FP, and FN are 58.4, 60.8, 3.2, and 5.6, respectively. Meanwhile, the averages of RE and PR are calculated to be 91.25% and 94.76%, respectively. Recall is less than precision, that is, the misjudgment of fall is larger

TABLE II
TEST RESULTS OF BEDSIDE FALL EXPERIMENTS

Fold No.	*TP*	*TN*	*FP*	*FN*
1	61	63	1	3
2	60	62	2	4
3	60	61	3	4
4	58	61	3	6
5	53	57	7	11
Average	58.40	60.80	3.20	5.60

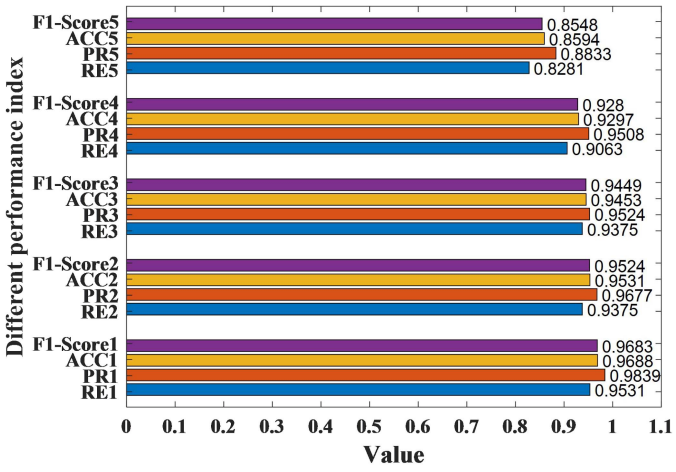

Fig. 16. Test results of four key performance indexes of 5-fold cross validation.

than that of nonfall. Finally, the averages of F1-Score and ACC are computed to be 92.97% and 93.13%, respectively.

On the other hand, as the ambient temperature rises, ACC decreases from 96.88% to 85.94%, and F1-Score decreases from 96.83% to 85.48%. As the ambient temperature rises, the difference between the ambient temperature and the body temperature will decrease, which affects the thermal image processing and recognition. When the ambient temperature is larger than 27 °C, ACC and F1-Score will drop fast.

V. CONCLUSION

In this article, a novel noncontact fall detector based on a MEMS thermopile Infrared array sensor and a radar sensor is developed to detect bedside falls. Besides, IR image processing algorithms based on the adaptive filter, successive approximation, double boundary scans, and mathematical morphology processing are proposed in detailed. The partition processing algorithm is used to suppress the influence of residual or existed heat sources on the bed or ground. Then, the statistical features of the center, area, temperature, and duration, as well as stable flag and fall action flag, are extracted for fall recognition. Finally, a three-layer RBF neural network is applied to distinguish the fall events from the nonfall events. Considering the influence factors of ambient temperature, brightness, gender, dressing, fall posture, fall location, and scenario, a total of 640 tests are conducted and 5-fold cross validation is used to evaluate the classification performance. Experimental results indicate that the averages of the recall, precision, $F1$-Score, and detection accuracy are measured to be 91.25%, 94.76%, 92.97%, and 93.13%, respectively, which verifies that the proposed fall detection method is effective. Besides, the detection accuracy decreases from 96.88% to 85.94% as the ambient temperature rises.

In a word, the proposed beside fall detection algorithms are easy to be realized in the edge-computing processor. Therefore, this IT noncontact fall detector can be widely applied for bedside fall detection at home, which is low cost, nonwearable, unobtrusive, noninvasive, and privacy-preserved. Considering that the factors affecting bedside fall detection are so complex in real life scenarios, more tests should be performed to verify the stability and applicability of the proposed method, which will be our next work.

REFERENCES

[1] *World Population Ageing*, United Nat., New York, NY, USA, 2015. [Online]. Available: http://www.un.org/en/development/desa/population/publications/pdf/ageing/WPA2015_Report.pdf
[2] S. Naja, M. M. E. D. Makhlouf, and M. A. H. Chehab, "An ageing world of the 21st century: A literature review," *Int. J. Community Med. Publ. Health*, vol. 4, no. 12, pp. 4363–4369, 2017.
[3] *Falls*, World Health Org., Geneva, Switzerland, 2018. Accessed: Jan. 15, 2018. [Online]. Available: http://www.who.int/mediacentre/factsheets/fs344/en/
[4] *WHO, Number of People Over 60 Years Set to Double by 2050; Major Societal Changes Required*. World Health Org., Geneva, Switzerland, 2015. [Online]. Available: https://www.who.int/mediacentre/news/releases/2015/ olderpersons-day/en/
[5] A. Ibrahim, K. Chaccour, A. Hassani, and E. Andres, "Bed-fall detection and prediction: A generic classification and review of bed-fall related systems," *IEEE Sensors J.*, vol. 21, no. 5, pp. 5678–5686, Mar. 2021.
[6] L. Ren and Y. Peng, "Research of fall detection and fall prevention technologies: a systematic review," *IEEE Access*, vol. 7, pp. 77702–77722, 2019.
[7] A. Singh, S. U. Rehman, S. Yongchareon, and P. H. J. Chong, "Sensor technologies for fall detection systems: A review," *IEEE Sensors J.*, vol. 20, no. 13, pp. 6889–6919, Jul. 2020.
[8] P. Vallabh and R. Malekian, "Fall detection monitoring systems: A comprehensive review," *J. Ambient Intell. Humanized Comput.*, vol. 9, pp. 1809–1833, Nov. 2018.
[9] E. Boutellaa, O. Kerdjidj, and K. Ghanem, "Covariance matrix based fall detection from multiple wearable sensors," *J. Biomed. Informat.*, vol. 94, Jun. 2019, Art. no. 103189.
[10] M. Nahian et al., "Towards an accelerometer-based elderly fall detection system using cross-disciplinary time series features," *IEEE Access*, vol. 9, pp. 39413–39431, 2021.
[11] H. A. Hashim, S. L. Mohammed, and S. K. Gharghan, "Accurate fall detection for patients with Parkinson's disease based on a data event algorithm and wireless sensor nodes," *Measurement*, vol. 156, May 2020, Art. no. 107573.
[12] T. B. Rodrigues et al., "Fall detection system by machine learning framework for public health," *Procedia Comput. Sci.*, vol. 141, pp. 358–365, Jan. 2018.
[13] X. Xi, W. Jiang, Z. Lü, S. M. Miran, and Z.-Z. Luo, "Daily activity monitoring and fall detection based on surface electromyography and plantar pressure," *Complexity*, vol. 2020, pp. 1–12, Jan. 2020.
[14] R. J. Fauziah, G. A. Mutiara, and P. Periyadi, "Smart tracking and fall detection for golden age's citizen," *Procedia Comput. Sci.*, vol. 161, pp. 1233–1240, Jan. 2019.
[15] V. Cotechini, A. Belli, L. Palma, M. Morettini, L. Burattini, and P. Pierleoni, "A dataset for the development and optimization of fall detection algorithms based on wearable sensors," *Data Brief*, vol. 23, Mar. 2019, Art. no. 103839.
[16] L. Panahi and V. Ghods, "Human fall detection using machine vision techniques on RGB-D images," *Biomed. Signal Process. Control*, vol. 44, pp. 146–153, Jul. 2018.
[17] F. Shu and J. Shu, "An eight-camera fall detection system using human fall pattern recognition via machine learning by a low-cost android box," *Sci. Rep.*, vol. 11, p. 2471, Jan. 2021.

[18] P. Y. Feng, J. J. Peng, J. P. Li, P. Yan, and B. Hu, "Design and development of the fall detection system based on point cloud," *Procedia Comput. Sci.*, vol. 147, pp. 271–275, Jan. 2019.
[19] X. Kong, Z. Meng, N. Nojiri, Y. Iwahori, L. Meng, and H. Tomiyama, "A HOG-SVM based fall detection IoT system for elderly persons using deep sensor," *Procedia Comput. Sci.*, vol. 147, pp. 276–282, Jan. 2019.
[20] K.-S. Song, Y.-H. Nho, and D.-S. Kwon, "Histogram based fall prediction of patients using a thermal imagery camera," in *Proc. URAI*, Jeju, South Korea, 2017, pp. 161–164.
[21] J. M. A. Morgado and A. König, "Low-power concept and prototype of distributed resistive pressure sensor array for smart floor and surfaces in intelligent environments," in *Proc. Multi-Conf. Syst. Signals Devices*, Chemnitz, Germany, 2012, pp. 1–6.
[22] Y. Wang, K. Wu, and L. M. Ni, "WiFall: Device-free fall detection by wireless networks," *IEEE Trans. Mobile Comput.*, vol. 16, no. 2, pp. 581–594, Feb. 2017.
[23] S. Matsuguma and A. Kajiwara, "Bathroom accident detection with 79GHz-band millimeter wave sensor," in *Proc. SAS*, 2019, pp. 1–5.
[24] B. Jokanović, M. Amin, "Fall detection using deep learning in range-doppler radars," *IEEE Trans. Aerosp. Electron. Syst.*, vol. 54, no. 1, pp. 180–189, Feb. 2018.
[25] Z. Liu, M. Yang, Y. Yuan, and K. Y. Chan, "Fall detection and personnel tracking system using infrared array sensors," *IEEE Sensors J.*, vol. 20, no. 16, pp. 9558–9566, Aug. 2020.
[26] C. Taramasco et al., "A novel monitoring system for fall detection in older people," *IEEE Access*, vol. 6, pp. 43563–43574, 2018.
[27] S.-Y. Chiu, J.-C. Hsieh, C.-I. Hsu, and C. Chiu, "A convolutional neural networks approach with infrared array sensor for bed-exit detection," in *Proc. ICSSE*, 2018, pp. 1–6.
[28] J. Adolf, M. Macas, L. Lhotská, and J. Dolezal, "Deep neural network based body posture recognitions and fall detection from low resolution infrared array sensor," in *Proc. BIBM*, 2018, pp. 2394–2399.
[29] K. Naito and Y. Ogawa, "Fall detection scheme based on temperature distribution with IR array sensor," in *Proc. ICCE*, 2020, pp. 1–5.
[30] Q. Liang, L. Yu, X. Zhai, Z. Wan, and H. Nie, "Activity recognition based on thermopile imaging array sensor," in *Proc. EIT*, 2018, pp. 770–773.
[31] Q. Guan, C. Li, X. Guo, and B. Shen, "Infrared signal based elderly fall detection for in-home monitoring," in *Proc. IHMSC*, 2017, pp. 373–376.
[32] S. Moulik and S. Majumdar, "FallSense: An automatic fall detection and alarm generation system in IoT-enabled environment," *IEEE Sensors J.*, vol. 19, no. 19, pp. 8452–8459, Oct. 2019.
[33] R. Jansi and R. Amutha, "Detection of fall for the elderly in an indoor environment using a tri-axial accelerometer and kinect depth data," *Multidimension. Syst. Signal Process.*, vol. 31, pp. 1207–1225, Jan. 2020.
[34] A. Makhlouf, I. Nedjai, N. Saadia, and A. Ramdane-Cherif, "Multimodal system for fall detection and location of person in an intelligent habitat," *Procedia Comput. Sci.*, vol. 109, pp. 969–974, Dec. 2017.
[35] Z. Chen and Y. Wang, "Infrared-ultrasonic sensor fusion for support vector machine-based fall detection," *J. Intell. Mater. Syst. Struct.*, vol. 29, no. 9, pp. 2027–2039, 2018.
[36] Y. Wu, Y. Su, R. Feng, N. Yu, and X. Zang, "Wearable-sensor-based pre-impact fall detection system with a hierarchical classifier," *Measurement*, vol. 140, pp. 283–292, Jul. 2019.
[37] C. H. He, J. W. Tan, X. L. Jian, G. X. Zhong, L. L. Cheng, and J. Z. Lin, "A smart flexible vital signs and sleep monitoring belt based on MEMS triaxial accelerometer and pressure sensor," *IEEE Internet Things J.* vol. 9, no. 15, pp. 14126–14136, Aug. 2022, doi: 10.1109/JIOT.2022.3146926.
[38] P. Mazurek, J. Wagner, and R. Z. Morawski, "Use of kinematic and mel-cepstrum-related features for fall detection based on data from infrared depth sensors," *Biomed. Signal Process. Control*, vol. 40, pp. 102–110, Feb. 2018.
[39] N. Zerrouki, F. Harrou, Y. Sun, and A. Houacine, "A data-driven monitoring technique for enhanced fall events detection," *IFAC PapersOnline*, vol. 49, no. 5, pp. 333–338, 2016.
[40] K. Singh, A. Rajput, S. Sharma, "Human fall detection using machine learning methods: A survey," *Int. J. Math., Eng. Manag. Sci.*, vol. 5, no. 1, pp. 161–180, 2020.
[41] J. M. Quero, M. Burns, M. Razzaq, C. D. Nugent, and M. Espinilla, "Detection of falls from non-invasive thermal vision sensors using convolutional neural networks," *Proceedings*, vol. 2, no. 19, pp. 1–10, 2018.
[42] M. Farsi, "Application of ensemble RNN deep neural network to the fall detection through IoT environment," *Alexandria Eng. J.*, vol. 60, pp. 199–211, Feb. 2021.
[43] A. Alarifi and A. Alwadain, "Killer heuristic optimized convolution neural network-based fall detection with wearable IoT sensor devices," *Measurement*, vol. 167, Jan. 2021, Art. no. 108258.
[44] Y. Chen, X. Kong, L. Meng, and H. Tomiyama, "An edge computing based fall detection system for elderly persons," *Procedia Comput. Sci.*, vol. 174, pp. 9–14, Oct. 2020.
[45] D. Mrozek, A. Koczur, and B. Malysiak-Mrozek, "Fall detection in older adults with mobile IoT devices and machine learning in the cloud and on the edge," *Inf. Sci.*, vol. 537, pp. 132–147, Oct. 2020.

Chunhua He received the B.S. degree in microelectronics from Sun Yat-sen University, Guangzhou, China, in 2010, and the M.S. and Ph.D. degrees in microelectronics from Peking University, Beijing, China, in 2013 and 2018, respectively.

He was an Engineer with the No.5 Electronics Research Institute, Ministry of Industry and Information Technology, Guangzhou, from 2013 to 2017. He was an Engineer with Midea Group, Foshan, China, from 2017 to 2019. He was a Senior Engineer with Guangzhou 37 Degree Smart Home Company Ltd., Guangzhou, from 2019 to 2021. He joined the School of Computer, Guangdong University of Technology, Guangzhou, in 2021, where he is currently an Associate Professor. His current research interests include the design and application of MEMS sensors, artificial intelligence algorithms, and biomedical engineering.

Shuibin Liu received the B.S. degrees in computer science and technology from Guangzhou University Sontan College, Guangzhou, China, in 2022. He is currently pursuing the M.S. degree in artificial intelligence with the School of Computer, Guangdong University of Technology, Guangzhou.

His research interests include fall detection, MEMS application, snore recognition, pattern recognition, knowledge graph, and prognostics health management.

Guangxiong Zhong received the B.S. degree in electronic information engineering from Shantou University, Shantou, China, in 2009. He is currently pursuing the M.S. degree in technology economy and management with the South China University of Technology, Guangzhou, China.

He was an Engineer with Guangzhou Southern Power Group Technology Development Company Ltd., Guangzhou, from 2009 to 2015. He was an Engineer with Guangdong Hengju Medical Technology Company Ltd., Guangzhou, from 2015 to 2017. He was an Engineer with Midea Group, Foshan, China, from 2017 to 2019. He was a Senior Engineer of Guangzhou 37 Degree Smart Home Company Ltd., Guangzhou, from 2019 to 2021. He is currently a Senior Engineer of Guangdong University of Technology, Guangzhou. His current research interests include embedded intelligent product design, design and application of multisensor fusion algorithms, and artificial intelligence algorithms in biomedical engineering.

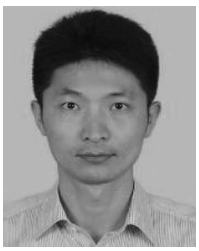

Heng Wu received the B.S. degree in electronic and information engineering from Wuhan University of Science and Technology, Wuhan, China, in 2009, and the M.S. and Ph.D. degrees in optics and mechanical manufacture and automation from the South China University of Technology, Guangzhou, China, in 2012 and 2017, respectively.

He is currently an Associate Professor with the School of Automation, Guangdong University of Technology, Guangzhou. His research interests are in the fields of optical imaging, optical measurement, machine vision, and image processing.

Lianglun Cheng received the B.S. and M.S. degrees in automatic control engineering from Huazhong University of Science and Technology, Wuhan, China, in 1988 and 1992, respectively, the Ph.D. degree in automatic control engineering from the Institute of Automation, Chinese Academy of Sciences, Beijing, China, in 1999.

He joined the School of Computer, Guangdong University of Technology, Guangzhou, China, in 1992, where he is currently a Professor and the Dean. His current research interests include Internet of Things and information physical integration system, interconnection and fusion of heterogeneous network, big data of industrial process, and high-performance computing.

Prof. Cheng is currently an Expert with special subsidy from the Government of the State Council, the Director of the national and local joint Engineering Research Center for integrated technology of Intelligent Manufacturing Information Physics Fusion System, Key Laboratory of Guangdong Information Physics fusion system, and China Automation Society, and the Deputy Director of Qian Xuesen Innovation Committee of CASS, a member of China Computer Society, the Vice director of Guangdong Automation Society, and the Executive Vice President of Guangdong Robotics Society.

Guizhen Yan received the B.S. degree in semiconductor from Peking University, Beijing, China, in 1974.

She is a Senior Visiting Scholar with Hong Kong University of Science and Technology, Hong Kong, from 1999 to 2001. She joined the National Key Laboratory of Science and Technology on Micro/Nano Fabrication, Institute of Microelectronics, Peking University, in 1974, where she is currently a Professor. She is the Founder of China's MEMS process technique and an expert in MEMS inertial sensors. She is Proficient in the techniques of microelectronic devices and IC manufacturing, and has developed several sets of CMOS and MEMS process techniques. In the 1970s, she participated in the development of China's first VLSI. In the 1980s, she developed a complete set of process technique for polysilicon emitter-stage ultrahigh-speed two-stage integrated circuits. She has developed the single-chip integration techniques for bulk silicon MEMS and CMOS. She has more than 40 invention patents and has published more than 200 papers in magazines and conferences. Her current research interests include the design and application of integrated circuit, MEMS process, and MEMS inertial sensor.

Yangxing Wen received the M.D. degree (8-year program) from Sun Yat-sen University, Guangzhou, China, in 2014.

He has been working with the First Affiliated Hospital of Sun Yat-sen University, since 2014, where he is currently an Attending Doctor. He is currently specialized in reproductive endocrinology and assisted reproductive technology. His clinical and research interests include polycystic ovary syndrome, assisted reproductive technology, and application of AI in health management and medicine.